ORIGINAL ARTICLE

Novel hybrid informational model for predicting the creep and shrinkage deflection of reinforced concrete beams containing GGBFS

Iman Faridmehr[1] · Mohd Shariq[2] · Vagelis Plevris[3] · Nasrin Aalimahmoody[4]

Abstract
This study investigates a Novel Hybrid Informational model for the prediction of creep and shrinkage deflection of reinforced concrete (RC) beams containing different percentages of ground granulated blast furnace slag (GGBFS) at different ages, varying from 1 to 150 days. The percentage of cement replacement by GGBFS varies from 20 to 60%. In order to examine the effects of the applied load and tensile reinforcement on creep behavior, the magnitude of two-point loading was varied from 200 kg to a maximum of 350 kg while the percentage of tensile reinforcement (ρ) was selected as either 0.77% or 1.2%. The current situation about short-term and long-term deflections due to creep and shrinkage available in the international standards, including ACI, BS and Eurocode 2, is discussed. The results indicate that RC beams containing GGBFS have larger deflections than the ones with conventional concrete (i.e., ordinary Portland cement concrete). After 150 days, the average creep deflection of RC beams containing 20, 40, and 60% GGBFS was 30, 70, and 100% higher than the ones for conventional concrete beams, respectively. A hybrid artificial neural network coupled with a metaheuristic Whale optimization algorithm has been developed to estimate the overall deflection of concrete beams due to creep and shrinkage. Several statistical metrics, including the root mean square error and the coefficient of variation, revealed that the generalized model achieved the most reliable and accurate prediction of the concrete beam's deflection in comparison with international standards and other models. This novel informational model can simplify the design processes in computational intelligence structural design platforms in future.

Keywords GGBFS · Creep and shrinkage deflection · Neural networks · Whale optimization algorithm

✉ Vagelis Plevris
vplevris@qu.edu.qa

Iman Faridmehr
s.k.k-co@live.com

Mohd Shariq
mshariqdce@gmail.com

Nasrin Aalimahmoody
mahmoody.elec@gmail.com

[1] South Ural State University, Lenin Prospect 76, 454080 Chelyabinsk, Russia

[2] Department of Civil Engineering, Z.H. College of Engineering and Technology, Aligarh Muslim University, Aligarh 202001, India

[3] Department of Civil and Architectural Engineering, College of Engineering, Qatar University, Doha, Qatar

[4] Department of Electrical Engineering, Yazd Branch, Islamic Azad University, Yazd, Iran

1 Introduction

The worldwide construction of various types of structures relies heavily on concrete. Nevertheless, the presence of ordinary Portland cement (OPC) as a binder constituent in concrete is still a major concern because of the significant carbon dioxide (CO_2) emissions and embodied energy associated with it. Cement production accounts for approximately 7% of the global CO_2 emissions produced by the construction industry [1–5]. To alleviate this problem, scientists, engineers, and researchers have been continuously dedicating their efforts in developing novel and more sustainable construction materials using alternative types of binders.

Recently there has been increasing research and production of green concrete, an eco-friendly alternative to ordinary Portland cement concrete (OPCC) [6, 7]. Vast quantities of industrial by-products are produced annually, and instead of treating them as waste material, these by-products can be used in the concrete industry, to produce the so-called green concrete. Many industrial by-products have been reported in the literature. Ground granulated blast furnace slag (GGBFS) -based concrete has received much attention because of its favorable properties, such as rapid strength gain, sulphate and acid attack resistance. The application of GGBFS as a binder constituent in concrete increases its compressive strength. This is due to the improvement of the structuring of poorly arranged microstructure, effects of pores filling, and twin creations formed during calcium silicate hydrate (C–S–H) gels, and extremely polymerized units of alkali-activation [8–10].

Although green concrete is a potential alternative as a sustainable construction material, the current application of green concrete in the construction industry is limited, possibly due to the lack of relevant design standards. Long-term deflections generated by drying shrinkage and creep in reinforced concrete (RC) beams pose a significant problem and need to be determined accurately. The long-term deflection of concrete under loading is referred to as *creep*, while the deformation of unloaded concrete is referred to as *shrinkage*. The four main types of shrinkage are autogenous shrinkage (caused by self-desiccation during concrete hydration), plastic shrinkage (caused by moisture loss from the concrete before setting), carbonation shrinkage (caused by the chemical reactions between hydrated concrete and CO_2 in the atmosphere), and drying shrinkage (as a result of the long-term dehydration of concrete over a long period). Shrinkage and creep are crucial to the long-term serviceability, long-term stability, durability, and safety of concrete structures. Although these long-term mechanical properties are fundamental from a structural design point of view, far too little research has been conducted on evaluating the drying shrinkage and creep behavior of RC beams containing industrial byproducts admixtures, such as GGBFS.

Previous research has shown that these long-term mechanical properties vary with the mix proportion, types of binder materials, and concrete curing method [11–13]. Hardjito et al. [14] tested fly ash-based geopolymer concrete (GPC) where the results confirmed low creep and slight drying shrinkage. In another experimental study, Collins and Sanjayan [15] suggested that larger creep and drying shrinkage can be achieved by alkali-activated slag concrete, compared to OPCC. Li and Yao's study [16] of the effects of silica fume and ultra-fine GGBFS on the drying shrinkage and creep characteristics of high-performance concrete suggested that GGBFS/silica fume improved concrete drying-shrinkage and achieved creep values that were relatively lower than the ones of traditional high-strength concrete. The effect of curing methods such as compound curing, moist curing, and air-dry curing on autogenous and drying shrinkage in normal and light-weight high-performance concrete was investigated by Nassif et al. [17]. The results of this study confirmed that the moist curing method after concrete casting improves the autogenous-shrinkage performance. In addition, in concrete mixes with very low water to binder ratios, both light-weight aggregates and fly ash were found to improve the autogenous shrinkage. The autogenous shrinkage in OPCC and silica-fume concrete with different water to binder ratios and silica-fume contents was investigated by Zhang et al. [18]. They concluded that autogenous shrinkage rose with increasing silica-fume content and decreasing water to binder ratios. In addition, the autogenous shrinkage strains of silica-fume concrete with low water to binder ratios developed more rapidly than the ones of the other specimens. The development of drying shrinkage and strength in self-consolidating concrete containing GGBFS, fly ash, silica fume, and metakaolin was investigated by Güneyisi et al. [19]. The results of the study confirmed that increasing fly ash content led to a slight reduction in the compressive strength, while specimens prepared with silica-fume and metakaolin provided higher compressive strength. In addition, replacing OPC with fly ash, GGBFS, and metakaolin reduced the drying shrinkage of self-consolidating concrete, while replacing PC with silica-fume increased the drying shrinkage. The effects of paste volume and cement type on the compressive strength, elastic modulus, creep, drying shrinkage, and stress development in self-consolidating concrete were investigated by Leemann et al. [20]. They concluded that these two variables influence creep and shrinkage significantly. Using experimental tests and analytical approaches, Huo et al. [21] investigated the modulus of elasticity, creep, and shrinkage of high-performance concrete. They concluded

that the shrinkage and creep of high-performance concrete were lower than the ones of OPCC and developed very rapidly, at early stages.

During the last decade, several authors have studied the time-dependent deflection of RC members. Zhou and Kokai [22] developed a simplified method to estimate the incremental deflection of RC members. They developed a methodology to estimate the incremental long-term deflection based on the recommendations of the Canadian design code. Mari et al. [23] developed a simplified technique for estimating the time-dependent deflection of RC beams. They considered constant stress in the tensile reinforcement subjected to sustained loading, the influence of exposure conditions, compressive strength, and the effect of compression reinforcement. In other studies, Mendis et al. [24] examined the long-term deflection behavior of composite steel–concrete beams, Xu et al. [25] developed a methodology for calculating shrinkage and creep deflections of RC beams, Hariche et al. [26] investigated the flexural performance of concrete beams, while Mias et al. [27] investigated the long-term performance of concrete beams with GFRP reinforcement for a period of 250 days. Shariq et al. [28] performed an experimental investigation to examine the effect of magnitude of sustained loading on long-term deflection of RC beams. In another experimental study conducted by Shariq et al. [29, 30], the effect of GGBFS on the long-term deflection of simply supported RC beams under two-point sustained load was examined. A comprehensive experimental study was conducted to examine the creep and shrinkage deflection of RC beams containing GGBFS as a partial replacement of cement by testing RC beams of three design mixes, two percentages of tensile reinforcement, and different magnitudes of sustained loading. Un [31] investigated the time-dependent behavior of geopolymer RC beams, while Mias et al. [27] tested RC beams with different percentages of GFRP and steel rebars subjected to sustained loads.

Several researchers have employed artificial intelligence techniques to estimate the creep and shrinkage deflection of reinforced concrete structures. A new computational framework for Bayesian inference regarding the long-term deflection of concrete structures was proposed by Han et al. [32]. The importance-sampling technique and the response surface method were involved in improving the efficiency and stability of the computation. Al-Zwainy et al. [33] investigated the use of ANNs to predict the time-dependent deflection of reinforced concrete beams and compared their predictions with the ones obtained by several existing time-dependent deflection experimental data. They concluded that to accurately predict the time-dependent deflections at any time of the service life of concrete beams, the effect of several parameters, such as concrete compressive strength,

the ratio of flexural reinforcement, environmental condition, creep coefficient, and shrinkage strain, should be considered. Zhu and Wang [34] proposed models of creep and shrinkage based on convolutional neural networks where the performance was verified by using 906 sets of creep experiment data and 1114 sets of shrinkage experiment data in the Northwestern University database. Over simulating creep and shrinkage in simply supported reinforced concrete beams, the comparison results of long-term deformation showed that the maximum error was caused by various factors such as environmental fluctuations and the error of models. Nguyen et al. [35] developed a hybrid data-driven method that employs the extreme gradient boosting machine and the particle swarm optimization metaheuristic to predict long-term deflections of reinforced-concrete members. A machine learning technique generalizes a nonlinear mapping function that helps infer long-term defection results from the input data whereas, a swarm-based metaheuristic aims at optimizing the machine learning model by fine-tuning its hyper-parameters. Although various models have been developed to predict the creep and shrinkage of concrete, more accurate and reliable prediction methods are still needed as the precise estimation of these parameters can significantly enhance the effectiveness of structural maintenance processes.

Real-world engineering problems are required to be solved today as the world is shifting very fast in technological features [36]. The majority of these problems are high-dimensional and challenging global optimization problems [37], making them extremely hard to solve as an increase in the problem's dimensionality rapidly increases the size of the search space [38]. Gradient-based and other traditional optimization techniques have proven ineffective in solving these complex problems for several reasons, including the so-called "curse of dimensionality". Furthermore, searching using the gradient-based techniques for engineering problems with the local solution is relatively time-consuming as these techniques rely on and depend on the position of an initial point [39]. All these drawbacks have encouraged researchers to develop new novel optimization approaches such as metaheuristics or hybrid methodologies [40] to optimize real-world engineering problems [41]. Metaheuristic optimization algorithms are becoming more and more prevalent in engineering applications as they: (i) are rather easy to implement and rely on relatively simple concepts; (ii) can avoid local optima; (iii) do not require gradient information; and (iv) can be applied in a wide range of problems covering different disciplines. Whale Optimization Algorithm (WOA) is an optimization algorithm developed by Mirjalili and Lewis [42]. As a swarm intelligence algorithm proposed for handling continuous optimization problems, WOA has shown remarkably good performance in a variety

of problems. WOA is inspired by the hunting attitude of the humpback whales, where each solution is thought to be a whale. In this solution, a whale tries to replete a new place in the search space, considered the best element of the group as a reference. Whales have used two mechanisms for searching the prey location and attack. In the first strategy, preys are encircled, and subsequently, the whale creates bubble nets following the second strategy [43].

More recent research has focused on experimentally evaluating the creep and shrinkage deflection of RC beams with and without admixtures. Only limited information is available on the prediction of creep and shrinkage deflection of RC beams containing GGBFS. The predicted models can play an important role in improving the design and reducing construction time. Therefore, to address the issue of limited information in the literature on the prediction of long-term deflection of green concrete (i.e., GGBFS based concrete), a hybrid artificial neural network coupled with a metaheuristic Whale optimization algorithm (WOA) was proposed to estimate the overall deflection (i.e., sum of instantaneous or elastic, creep and shrinkage) of RC beams containing GGBFS. Experimental data on the creep and shrinkage deflection of RC beams containing GGBFS, presented in earlier studies of the authors [29, 30], have been used for the analysis and the development of the prediction model. The current situation about short-term and long-term deflections due to creep and shrinkage available in international standards is also discussed in detail. The proposed hybrid artificial neural network model considers various key RC beam parameters. Several statistical metrics have been used for ensuring the robustness and reliability of the proposed methodology against test results and international standard models.

2 State of the art

2.1 Existing methods for estimating long-term deflection of RC beams due to creep and drying shrinkage

This section presents the current state of the art and investigates the empirical equations recommended by international standards for estimating short and long-term deflections of RC beams due to creep and drying shrinkage.

2.1.1 Short-term deflection

The short-term deflection is defined as the initial elastic deflection produced by the instantaneously applied load. If the magnitude of the sustained load is low, the section is considered uncracked, and therefore the elastic theory can be used to estimate the short-term deflection as follows.

$$\delta_i = \frac{Pa}{24E_c I_g}\left(3l^2 - 4a^2\right) \tag{1}$$

where P is the magnitude of the concentrated load applied on the beam, a is the distance between the support and the concentrated load, E_c is the modulus of elasticity of concrete at the loading age, I_g is the gross moment of inertia of the RC beam cross section, and l is the effective span of the beam.

The cross section properties of the RC beam with overall depth D and width b are given in Table 1 for the different standards.

In the formulas of Table 1, f_c is the cube compressive strength at 28 days, f_c' is the cylinder compressive strength at 28 days, K_0 is a constant related to the modulus of elasticity of aggregate, taken as 20 kN/mm² for normal strength concrete, z is the lever arm, x is the depth of neutral axis, d is the effective depth, A_s is the area of tension steel, a_e is the modular ratio, y_t is the distance from the neutral axis to the extreme tension face, and M is the maximum moment under service load.

2.1.2 Long-term deflection

The procedure to estimate the drying shrinkage and creep deflection recommended by different design codes is discussed in this section.

2.1.2.1 American Concrete Institute (ACI 318-19) Following ACI 318-19 [44], additional time-dependent deflection resulting from creep and shrinkage of flexural members shall be calculated as the product of the immediate deflection caused by sustained load and the factor λ_Δ given by

$$\lambda_\Delta = \frac{\lambda}{1 + 50\rho'} \tag{2}$$

where λ is the time-dependent multiplier given in Table 2, and ρ' is the ratio of A_s' to bd. Eq. (2) was developed by Branson and Christiason [47], where the term $(1 + 50\rho')$ accounts for the effect of compression reinforcement in reducing the time-dependent deflections.

2.1.2.2 British Standard (BS 8110) The BS 8110 standard [45] considers the classical modular ratio method to estimate the long-term deflection due to creep, excluding shrinkage effects [48], as follows

$$\delta_c = Kl^2 \frac{1}{r_c} \tag{3}$$

where K is a constant depending on the support condition, and $1/r_c$ is the curvature due to creep, which can be computed as $\frac{M}{E_{eff} I_g}$.

Table 1 Cross section properties of RC beam

Design code	Modulus of elasticity of concrete, E_c (MPa)	Moment of inertia (MI) of RC beam section	Cracking moment, M_{cr}	Modulus of rupture of concrete, f_{cr}
ACI 318-19 [44]	$E_c = 4700\sqrt{f_c'}$	Effective MI $I_{eff} = \left(\frac{M_{cr}}{M}\right)^3 I_g + \left(1 - \left(\frac{M_{cr}}{M}\right)^3\right) I_{cr}$	$M_{cr} = \frac{f_{cr} I_g}{y_t}$	$f_{cr} = 0.62\sqrt{f_c'}$
BS 8110 [45]	$E_c = K_0 + 0.2 f_c$	Cracked MI $I_{cr} = 0.34 b x^3 + a_e A_s (d - x)^2$ Un-cracked MI $I_g = \frac{bD^3}{12} + bD\left(\frac{D}{2} - x\right)^2 + a_e A_s (d - x)^2$	–	–
Eurocode 2 [46]	$(E_c)_{28} = 9.975(f_c + 8)^{0.33}$	Cracked MI $I_{cr} = \frac{bx^3}{3} + a_e A_s (d - x)^2$ Un-cracked MI $I_g = \frac{bD^3}{12} + bD\left(\frac{D}{2} - x\right)^2 + (a_e - 1) A_s (d - x)^2$	$M_{cr} = \frac{f_{cr} I_g}{h - x_u}$	$f_{cr} = 0.3 f_c^{0.67}$

Table 2 Time-dependent factor for sustained loads recommended by ACI 318

Duration of sustained load (days)	Time-dependent multiplier, λ
10	0.11
30	0.36
90	1.00
120	1.13
150	1.17

BS 8110 recommends the following equation to estimate the deflection due to shrinkage, using the moment–curvature relationship theorem.

$$\delta_s = K l^2 \frac{1}{r_s} \tag{4}$$

where $1/r_s$ is the curvature due to shrinkage, calculated by

$$\frac{1}{r_s} = \frac{\varepsilon_s a_e s_u}{I_g} \tag{5}$$

where ε_s is the free shrinkage strain, S_u is the first moment of area of the reinforcement about the centroid of the section, $A_s(d - x)$, I is the second moment of area of the section, and a_e is the effective modular ratio, $\frac{E_s}{E_{eff}}$.

2.1.2.3 Eurocode 2 (EN 1992-1-1:2004) Eurocode 2 [46] considers the curvature method to estimate the long-term deflection resulting from creep and shrinkage, using the following equation

$$\delta_t = K l^2 \frac{1}{r_t} \tag{6}$$

where $1/r_t$ is the total curvature due to creep and shrinkage, equal to $\frac{1}{r_c} + \frac{1}{r_s}$; defined in Eqs. (3) and (5).

2.2 Experimental program

The experimental data on the creep and shrinkage deflection of RC beams containing GGBFS, presented in earlier studies of the authors [29, 30], have been used for the analysis and the development of the prediction model of the present study.

2.2.1 Materials and sample preparation

The locally available river sand retained on IS sieve #15 (150-micron size) and passing through IS sieve #480 (aperture 4.75 mm square) was selected as fine aggregate, according to IS 383 [49]. The crushed stone aggregate prepared from quartzite rock with a maximum nominal size of 16 mm was selected as coarse aggregate. The physical properties of the fine and coarse aggregates are presented in Table 3.

OPC grade 43, in accordance with IS 4031 [50] and the GGBFS procured from the Indorama cement industry, Raipur, Maharashtra, India in compliance with IS 8112 [51], were selected as concrete binders in the experiments. The mechanical properties of the selected aggregates (including setting time, compressive strength), OPC, and GGBFS addressed the requirements of the relevant code specifications, including IS 383 [49], IS 456 [52], IS 4031 [50], and IS 12089 [53]. For the tensile reinforcement, thermo-mechanically treated (TMT) steel rebars with 8 and 10 mm nominal diameter, 445 MPa yield strength, and 561 MPa ultimate strength were used.

Table 3 Physical properties of fine and coarse aggregates

Characteristic	Fine aggregate	Coarse aggregate
Grading	Zone-II of (IS 383) [49]	–
Fineness modulus	2.45	6.8
Specific gravity	2.61	2.63
Density (Loose) (kN/m^3)	15.4	14.3
Water absorption (%)	0.85	1.5

2.2.2 Mixture proportions

In the experiments, three groups of concrete mixes designated as M1, M2 and M3 (with four mixes in each group) were prepared by varying the percentages of binder mass, as shown in Table 4 and considered in earlier studies by the authors [54]. In each group, the fine aggregate to coarse aggregate ratio was kept constant at 0.6 to address the maximum density of combined aggregate, while the water to binder ratio varies between 0.45 to 0.55. Three OPCC mixes are considered, designated as M10, M20 and M30, with 28 days cube (150 mm) compressive strength of 46.51, 37.03 and 27.09 MPa, respectively. The OPC was replaced by 20, 40, and 60% GGBFS in OPCC mixes to prepare GGBFS based modified concretes. The Mix ID in Table 4 (for example, M32) is defined as follows: the first term (M1) represents the mix group (1, 2, or 3), the second term (2 in M32) indicates the percentage replacement of GGBFS where 0 means 0% GGBFS, 1 means 20% GGBFS, 2 means 40% GGBFS and 3 means 60% GGBFS.

2.2.3 Test specimens and loading protocol

Figure 1 shows the geometry of the tested specimens and the test setup for the measurement of the long-term deflection due to shrinkage and creep. Two OPCC beams of each mix group (M10, M20, and M30) of size $100 \times 150 \times 1800$ mm $(B \times D \times L)$ were tested to determine the first crack load. The first crack load and the ultimate load carrying capacity of the specimens are presented in Table 5, where the sustained load for creep deflection of GGBFS modified concrete was taken as 25% of these first crack loads.

To record the creep deflection, the sustained two-point load was applied on the RC beams of size $100 \times 150 \times 1800$ mm $(B \times D \times L)$ at the age of 28 days using different weight of blocks of concrete, as shown in Fig. 1. The schematic diagram of RC beam geometry and reinforcement detailing is also shown in Fig. 1. To measure the mid-span deflection, a dial gauge with a least count of 0.01 mm was mounted at the mid-span of the RC beam. The position of the specimens during the test was controlled in a regular basis and the tests were performed at ambient temperature (27 ± 2 °C) with relative humidity 60–65%. Once the sustained two-point load

Table 4 Concrete mix properties [54]

Mix group	Mix ID	GGBFS replacement (%)	Cement (kg/m^3)	GGBFS (kg/m^3)	FA (kg/m^3)	CA (kg/m^3)	w/b ratio	Slump (mm)	CF	28-day cube compressive strength (MPa)
M1	M10	0	400	0	665	1107	0.45	41	0.90	46.51
	M11	20	320	80				43	0.90	38.38
	M12	40	240	160				49	0.92	35.22
	M13	60	160	240				51	0.91	30.14
M2	M20	0	350	0	680	1132	0.50	46	0.91	37.03
	M21	20	280	70				45	0.91	32.96
	M22	40	210	140				51	0.92	30.93
	M23	60	140	210				54	0.90	26.87
M3	M30	0	320	0	688	1145	0.55	51	0.92	27.09
	M31	20	256	64				53	0.93	24.51
	M32	40	192	128				59	0.95	22.80
	M33	60	128	192				61	0.96	18.97

FA Fine aggregate, *CA* coarse aggregate, *w/b* water to binder ratio, *CF* compaction factor

(a)

(b)
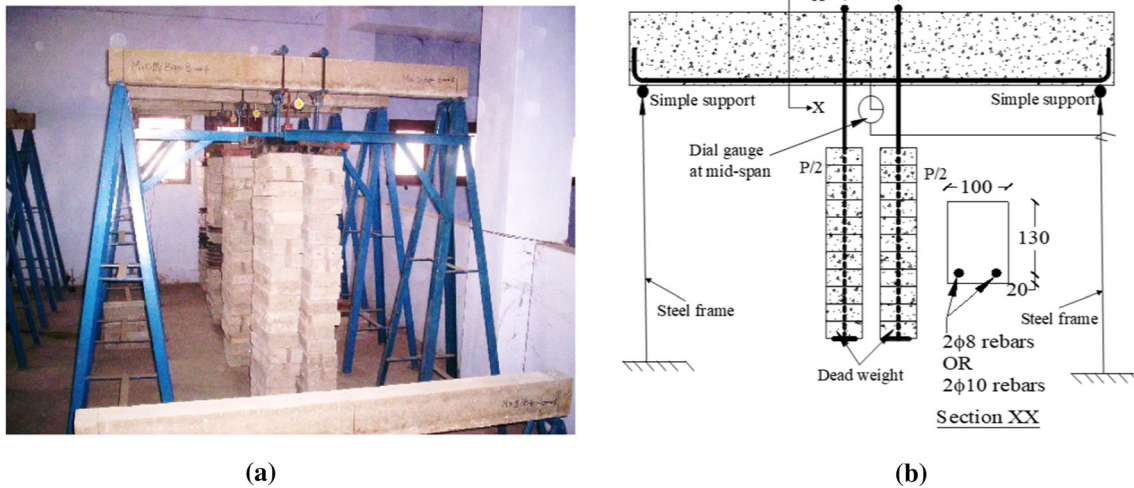
Fig. 1 **a** Creep and shrinkage deflection testing setup, **b** Specimen's geometry and reinforcement detailing

Table 5 First crack load and ultimate capacity of OPCC beams [29]

Mix	Average load at first crack (t)	Average ultimate load (t)
M10	1.2	2.1
M20	1.0	1.8
M30	0.8	1.5

was applied on the beams, the corresponding deflection was immediately recorded. The creep deflection was recorded at the time of 1, 3, 7, 14, 21, 30, 60, 90, 120, and 150 days after applying the sustained two-point load. No sign of cracking was observed in the specimens during the sustained loading test. To examine the effect of the tensile reinforcement percentage, a similar series of tests with the same beam geometry and loading protocol was performed; however, the reinforcement percentage ρ was increased from 0.77% (two 8 mm rebars) to 1.21% (two 10 mm rebars).

2.3 Discussion on the shrinkage and creep deflection of RC beams based on the experiment

All tested beams are unsymmetrical with respect to their centroid since the reinforcement rebars were only mounted at the bottom of the sections. Therefore, concrete in the compression zone shrunk more than the one in the tension zone, resulting in a downwards deflection. Figure 2 shows the development of shrinkage and creep deflection at different ages for all three mix designs with 8 mm rebars. Figure 3 shows the same for all three mix designs with 10 mm rebars. Considering specimens with 8 mm rebars,

the same behavior was observed where the rate of the overall deflection was increased by increasing the GGBFS replacement. By increasing ρ from 0.77% (two 8 mm rebars) to 1.21% (two 10 mm rebars), the overall deflection increased in all mix groups by an average of 17% due to an increase in the first crack load carrying capacity. Such an increase is more evident in design mixes that contain high content GGBFS (i.e., M13, M23, and M33).

A detailed description of the experimental setup and the corresponding test results can be found in some other works by the authors [29, 30]. The following points summarize the observations made in the experiments:

(i) On average, shrinkage was responsible for around 12% of the overall deflection of RC beams regardless of the binder constituents.

(ii) The shrinkage and creep deflection of all tested specimens increased with time. However, the rate of the overall deflection increased by increasing the GGBFS replacement. At the age of 150 days, the overall deflection of mix design M13 in the M1 mix group containing 60% GGBFS was 72% higher than the OPCC-based beam.

(iii) On average, 70% of the shrinkage deflection at the age of 150 days was achieved within 60 days, while this percentage increased to 73% for the creep deflection.

(iv) Decreasing the OPC content by 20% and increasing the water to binder ratio by 22% (mix group 1 to mix group 3) led to an increase in the overall deflection by 40% in OPCC based beam and by an average of 30% in GGBFS modified concrete beams. In other words, the creep and shrinkage deflection are inversely proportional to the compressive strength of concrete.
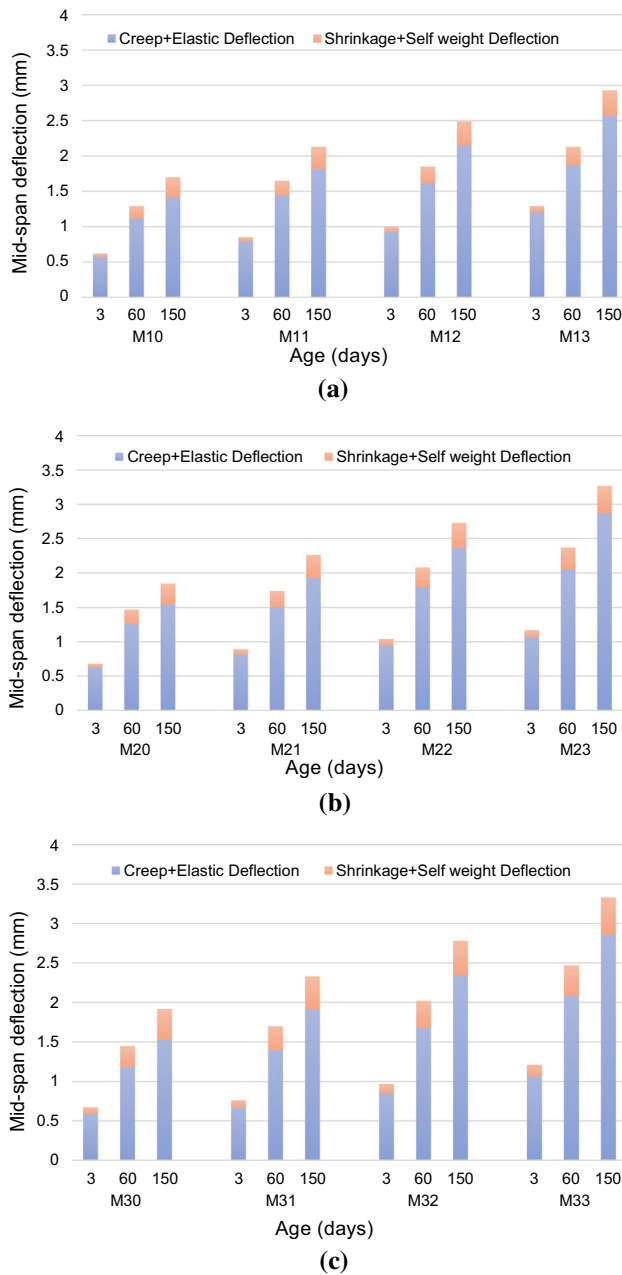
Fig. 2 Time-dependent shrinkage and creep deflection of RC beams with 8 mm rebars for different mix groups: **a** M1, **b** M2, **c** M3

3 Developing informational models to estimate the overall deflection of RC beams

To develop a reliable model for estimating the overall deflection of RC beams as a result of creep and shrinkage, it is imperative to elucidate the physical phenomena and the underlying mechanisms associated with the key geometrical and mechanical parameters involved. This study investigates the development of an informational model based on a hybrid ANN coupled with a Whale optimization
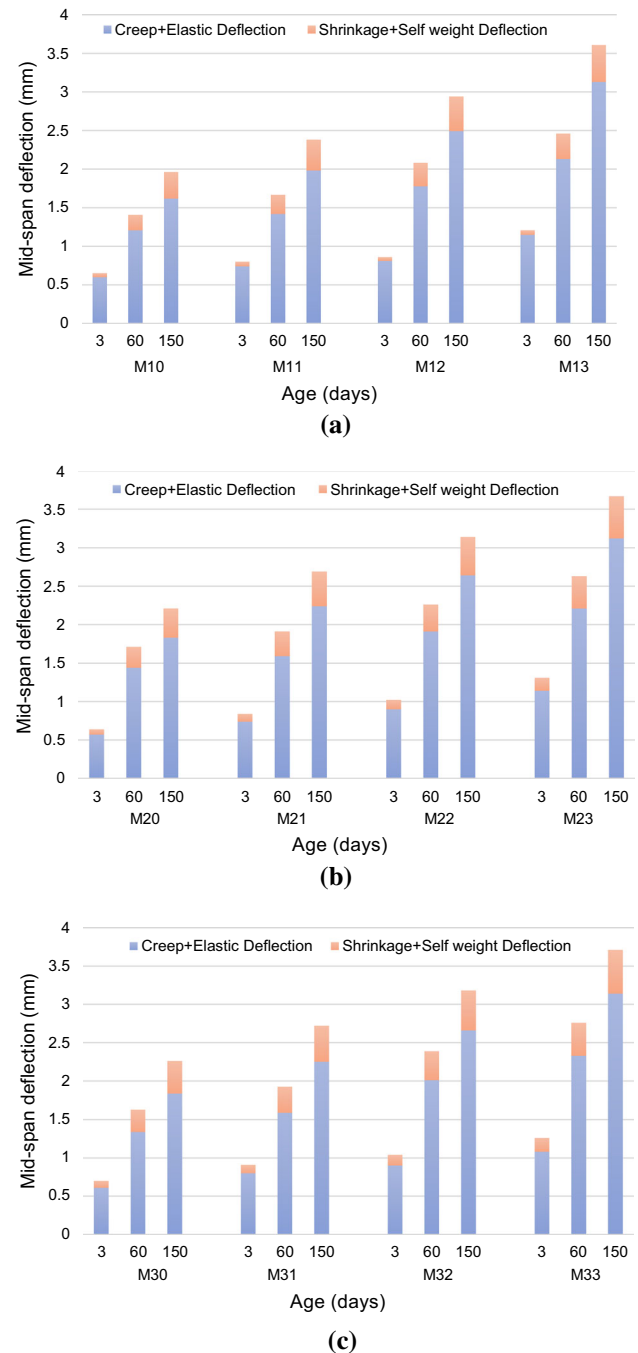
Fig. 3 Time-dependent shrinkage and creep deflection of RC beams with 10 mm rebars for different mix groups: **a** M1, **b** M2, **c** M3

algorithm. Using the comprehensive experimental dataset developed in this study, an informational model is developed to estimate the overall deflection as a result of creep and shrinkage determined by the fundamental geometrical and mechanical input parameters (GGBFS content, f_c', magnitude of the sustained load, area of tensile reinforcement, and time). ANN is a data processing system that learns from experience and can generalize its knowledge to

new data, unfamiliar to the model [55–57]. Inspired by the structure of the biological brain, ANN comprises a group of neurons that operate locally to solve a particular problem. Neural networks acquire knowledge through learning via a simplified human brain-like approach in customary computations that capture the underlying mechanisms in a dataset. The multilayer feed-forward network used in this study is a reliable and commonly used ANN architecture [58]. The multilayer feed-forward network comprises three types of layers: the input layer where the data are introduced to the model; the hidden layer(s) where the network processes the data; and subsequently, the output layer where the network results are obtained as outputs. Each layer consists of a group of nodes referred to as neurons that are connected to the neurons of the previous and the next layers. The neurons in the output and the hidden layers consist of three elements: an activation function, weights, and biases. Standard and commonly used activation functions include the nonlinear sigmoid functions (*logsig*, *tansig*) and linear functions (*poslin*, *purelin*) [59]. Training algorithms aim to optimize the weight and bias values by minimizing an error function. The backpropagation (BP) algorithm is one of the most reliable and widely used ANN training algorithms [60, 61].

3.1 Whale optimization algorithm

The Whale optimization algorithm (WOA) is a meta-heuristic optimization algorithm, imitating the hunting mechanism of humpback whales in the ocean, and was proposed by Mirjalili and Lewis [42]. The bubble-net feeding method employed by humpback whales is considered one of the most intelligent hunting techniques, as explained by Watkins and Schevill [62]. Humpback whales are interested in hunting small fish or schools of krill that swim close to the water surface. It has been observed that the hunting is done by creating distinctive bubbles along a 9'-shaped path or circle, as shown in Fig. 4a. Before 2011, this hunting behavior was only examined via surface observation. Goldbogen et al. [63] was the first to explore it utilizing tag sensors. They recorded 300 tag-derived bubble-net feeding events from nine individual humpback whales. They observed two maneuvers associated with producing bubbles: upward-spirals and double-loops. In the upward-spirals maneuver, humpback whales dive around 12-m down in the water, begin to produce bubbles in a spiral shape over the prey and then swim up to the water surface. The double-loop maneuver includes three distinctive phases: coral loop, lobtail, and capture loop. Detailed information about this hunting technique can be found in [63]. The spiral bubble-net feeding maneuver is mathematically simulated to perform optimization in this study [64]. A flowchart of the method is presented in Fig. 4b.

3.2 Production of training and testing data sets

To predict the creep and shrinkage deflection of RC beams containing different percentage of GGBFS at different ages (varying from 1 to 150 days), a dataset consisting of three mix designs was developed as discussed in a previous section. As mentioned earlier, the independent input parameters are the following: GGBFS content; compressive strength (f_c'); magnitude of sustained load; area of tensile reinforcement; and time, forming a 5×1 matrix while the dependent output parameter (the overall deflection i.e., summation of instantaneous + shrinkage + creep deflection) is a scalar value (1×1 matrix). The minimum and maximum values for each input variable along with other statistical properties are reported in Table 6, where STD stands for Standard Deviation.

In statistics, any statistical relationship, whether causal or not, between two random variables is called correlation or dependency. In the broadest sense, correlation refers to the degree to which a pair of parameters are linearly associated. A correlation matrix is a table that provides the correlation coefficients among the various input variables. Figure 5 shows the correlation matrix for the 6 (5 input and 1 output) variables of the study. Considering the range of data for each variable and to avoid any divergence in the results, the variables were first normalized in the range of − 1 to 1 using the following equation:

$$X_n = \frac{2(X - X_{\min})}{X_{\max} - X_{\min}} - 1 \tag{7}$$

where X_n is the normalized value of the variable in the region [− 1, 1], $X_{\max}$ is the maximum value of X, and $X_{\min}$ is its minimum value. X is the original (non-normalized) value of the variable.

The statistical behavior of the output parameter (the overall deflection) needs to be evaluated. For this purpose, a distribution plot is constructed as shown in Fig. 6. This plot reveals that the overall deflection is mainly distributed in the range of 0.5–2 mm.

A trial-and-error method is often employed to obtain the most efficient ANN model architecture that best reflects the characteristics of the experimental test data. In the present study, the number of neurons in the hidden layers is determined according to Eq. (8) [65, 66], where N_H is the number of neurons in the hidden layer(s), N_I is the number of input variables (i.e., 5) and N_{TR} is the number of training samples in the database (i.e., 70% out of 264 samples).

Fig. 4 a Spiral bubble-net feeding maneuver of humpback whales, and **b** optimization flowchart using WOA

(a)

(b)
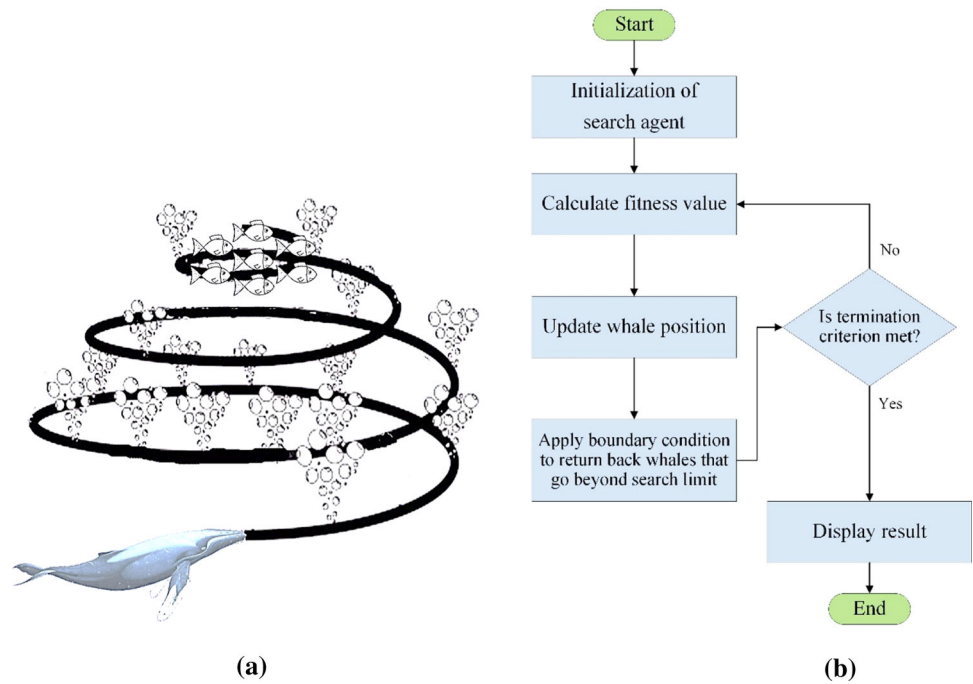
Table 6 Input and output variables' properties

Parameter	Unit	Type	Min	Max	Average	STD
GGBFS content	%	Input	0	60	30	22.4032
28-day cube compressive strength, f_c	MPa	Input	18.97	46.51	30.9508	7.31785
Area of tensile reinforcement	mm^2	Input	100.5	157.08	128.79	28.3437
Sustained two-point load	kg	Input	200	350	275	47.9623
Time (age)	days	Input	0	150	45.0909	50.3955
Creep + Shrinkage (C + S)	mm	Output	0.41	3.71	1.55708	0.765

Fig. 5 Correlation matrix for the 6 variables (5 input and 1 output variables)
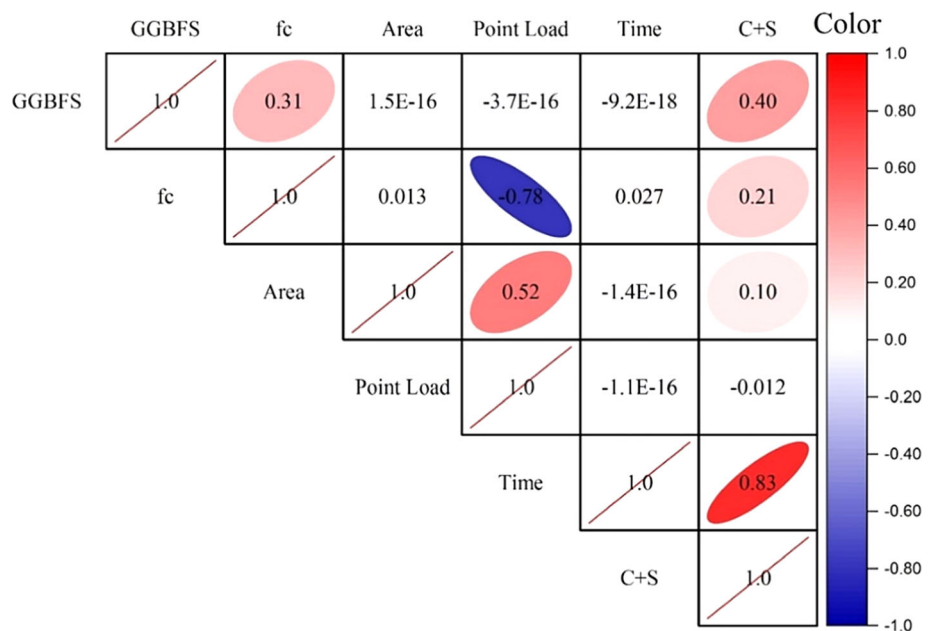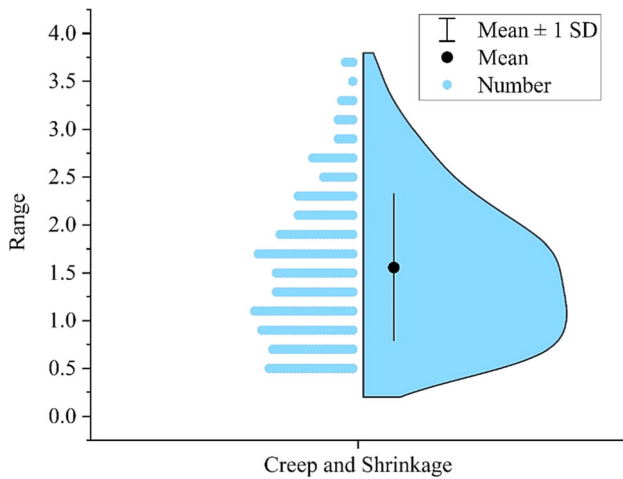
Fig. 6 Distribution plot for the output parameter (overall deflection)

$$N_{\mathrm{H}} \leq \min\left(2N_{\mathrm{I}} + 1; \frac{N_{\mathrm{TR}}}{N_{\mathrm{I}} + 1}\right) \tag{8}$$

Since the number of input variables is 5, the empirical equation reveals that the number of neurons in the hidden layers should be less than 11. Therefore, several networks with different topologies, with a maximum of two hidden layers and a maximum of 11 neurons at each hidden layer, were trained and examined in this study. The hyperbolic tangent transfer function and Levenberg–Marquardt training algorithm were used in all networks. Moreover, various statistical metrics, including the mean absolute relative error (MARE), coefficient of determination (R^2), variance accounted for (VAF), and mean squared error (MSE), which are expressed in Eqs. (9)–(10), were used to evaluate the performance of the different network topologies. In the following equations, A_i denotes the actual value, P_i denotes its prediction, n is the number of data points, $\overline{A}$ is the mean (average) of the actual values, function $var()$ denotes the variance of a variable, and function $covar()$ denotes the covariance of two variables.

$$MARE = \frac{1}{n}\sum_{i=1}^{n}\left|\frac{P_i - A_i}{A_i}\right| \tag{9}$$

$$MSE = \frac{1}{n}\sum_{i=1}^{n}(P_i - A_i)^2 \tag{10}$$

$$VAF = 1 - \frac{var(P - A)}{var(A)} \tag{11}$$

$$R^2 = \frac{(cov(P,A))^2}{var(P) \cdot var(A)} \tag{12}$$

In case of a perfect match between predicted and actual values, the metrics take the values $MARE = 0$, $MSE = 0$, $VAF = 1$ (or 100%), and $R^2 = 1$. In total, 12 different network topologies were examined, all having two hidden layers which is in general enough for handing such problems, according to the experience of the authors. It was found that the network with a 5–4–5–1-layer architecture achieved the lowest error values for MSE and the highest value of R^2 and VAF to estimate the output parameter (i.e., the overall deflection), as shown in Table 7.

Figure 7 illustrates the proposed 5–4–5–1 topology of the feed-forward neural network with two hidden layers, five input variables (neurons), and one output parameter.

The ANN used in this study was a feed-forward back-propagation network (newff in MATLAB), where 70% of the experimental data was used for training, and the remainder 30% was used for network testing. The Whale optimization algorithm was used to provide the least prediction error for the trained structure and to optimize the ANN's weights and biases. The parameters of the WOA used in the study are presented in Table 8.

3.3 Multiple linear regression and genetic algorithm models

To validate the proposed WOA-ANN model used in this study, a multiple linear regression (MLR) model and a genetic algorithm combined with an ANN (GA-ANN) were also developed. In an MLR model, two or more independent variables significantly affect the dependent variable, as shown in the following equation.

$$y = f(x_1, x_2, \ldots) \therefore \rightarrow y = a_0 + a_1 x_1 + a_2 x_2 + \cdots \tag{13}$$

where y is the dependent variable; x_1, x_2, …, are the independent variables; a_1, a_2, … are the linear equation coefficients.

MiniTab software has been used for developing the multiple linear regression models, where models having two and up to five independent variables were examined. The following equation shows the most suitable coefficients for the MLR model to estimate the overall deflection of the studied specimens, using five parameters.

$$Y = 0.344 + 0.01521X_1 + 0.0078X_2 + 0.00503X_3 \\ - 0.00255X_4 + 0.012589X_5 \tag{14}$$

where Y is the output (Creep and Shrinkage deflection), and the parameters X_1, X_2, X_3, X_4 and X_5 are the GGBFS (%), 28-day cube compressive strength (f_c), Area of tensile reinforcement in RC beams, Sustained two-Point Load and Time, respectively.

A genetic algorithm (GA) combined with an ANN (GA-ANN) was implemented for the second evaluation. The parameters of the method are presented in Table 9. A genetic algorithm is classified as a heuristic optimization approach. The algorithm mimics the process of natural evolution by adapting a population of individual solutions.

Table 7 Statistics of WOA-ANN algorithm on training and testing data

1st Layer	2nd Layer	1st TF	2nd TF	Training data (70%)				Test data (30%)			
				MSE	R^2	*MARE*	*VAF (%)*	*MSE*	R^2	*MARE*	*VAF (%)*
3	3	Tansig	Purelin	0.001	0.982	0.011	98	0.001	0.985	0.011	99
3	4	Purelin	Purelin	0.007	0.858	0.055	86	0.007	0.877	0.040	88
3	5	Poslin	Purelin	0.002	0.959	0.013	96	0.002	0.960	0.006	96
4	3	Logsig	Purelin	0.024	0.824	0.022	83	0.031	0.864	0.050	81
4	4	Tansig	Tansig	0.001	0.982	0.020	98	0.001	0.982	0.022	98
4	5	Tansig	Purelin	0.001	0.986	0.039	98	0.001	0.986	0.041	98
5	3	Purelin	Purelin	0.007	0.859	0.063	86	0.007	0.881	0.051	88
5	4	Poslin	Purelin	0.002	0.963	0.051	96	0.002	0.974	0.041	97
5	5	Logsig	Purelin	0.001	0.976	0.038	98	0.001	0.977	0.049	98
6	3	Tansig	Tansig	0.004	0.952	0.016	93	0.004	0.955	0.030	94
6	4	Tansig	Purelin	0.004	0.939	0.024	93	0.004	0.947	0.065	94
6	5	Tansig	Tansig	0.001	0.984	0.013	98	0.002	0.972	0.031	97

TF transfer function

Fig. 7 The proposed 5–4–5–1 topology of a feed-forward neural network
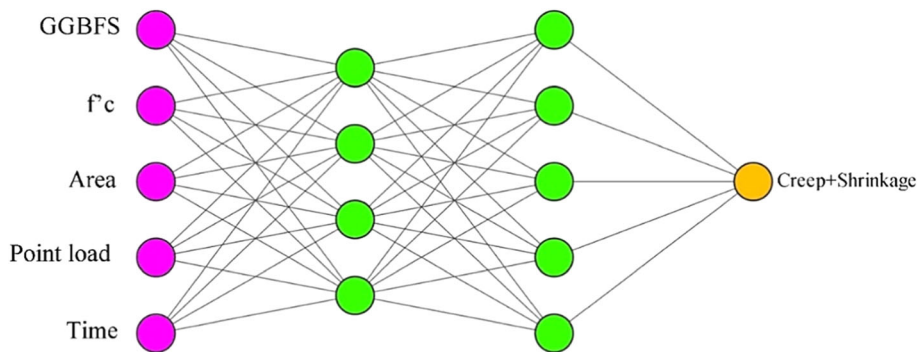
Table 8 WOA parameters used in the study

Parameter	Value
Lower limit of the optimization parameters (L_b)	− 0.2
Upper limit of the optimization parameters (U_b)	0.2
Search agents (N)	25
Loop counter (t)	0
Decrease linear (a)	2
Coefficient vectors (A)	− 0.8
Coefficient vectors (C)	+ 0.6

Table 9 Parameters of the Genetic Algorithm combined with ANN (GA-ANN)

Parameter	Value
Max generations	100
Recombination (%)	15
Lower/upper bound	[− 1, 1]
Crossover (%)	50
Crossover method	Single point
Selection method	Steady-State
Population size	150

GA randomly chooses individuals from the current population to be parents and applies various genetic operators to generate the next generation. Over consecutive generations, the population approaches an optimum solution as an evolutionary process and the principle of the "survival of the fittest". GA can be applied to solve various optimization problems in many applications that are not suited for conventional optimization methods.

3.4 Comparison of accuracy of informational models versus international standards

Figure 8 depicts a comparison between (a) the actual experimental data; (b) prediction of the novel WOA-ANN computational intelligence model developed in this study; (c) MLR; and (d) GA-ANN models, and the results from calculations based on the international standard design code models. Figure 8 indicates that the WOA-ANN model provided more reliable estimations of the overall deflection of RC beams compared to that of the MLR and GA-ANN models and also compared to the international standards.

Table 10 shows the statistical metrics of Eqs. (9)–(10), for all models. The results indicate that the proposed hybrid WOA-ANN model provided the most reliable results for the overall deflection of RC beams. The maximum values
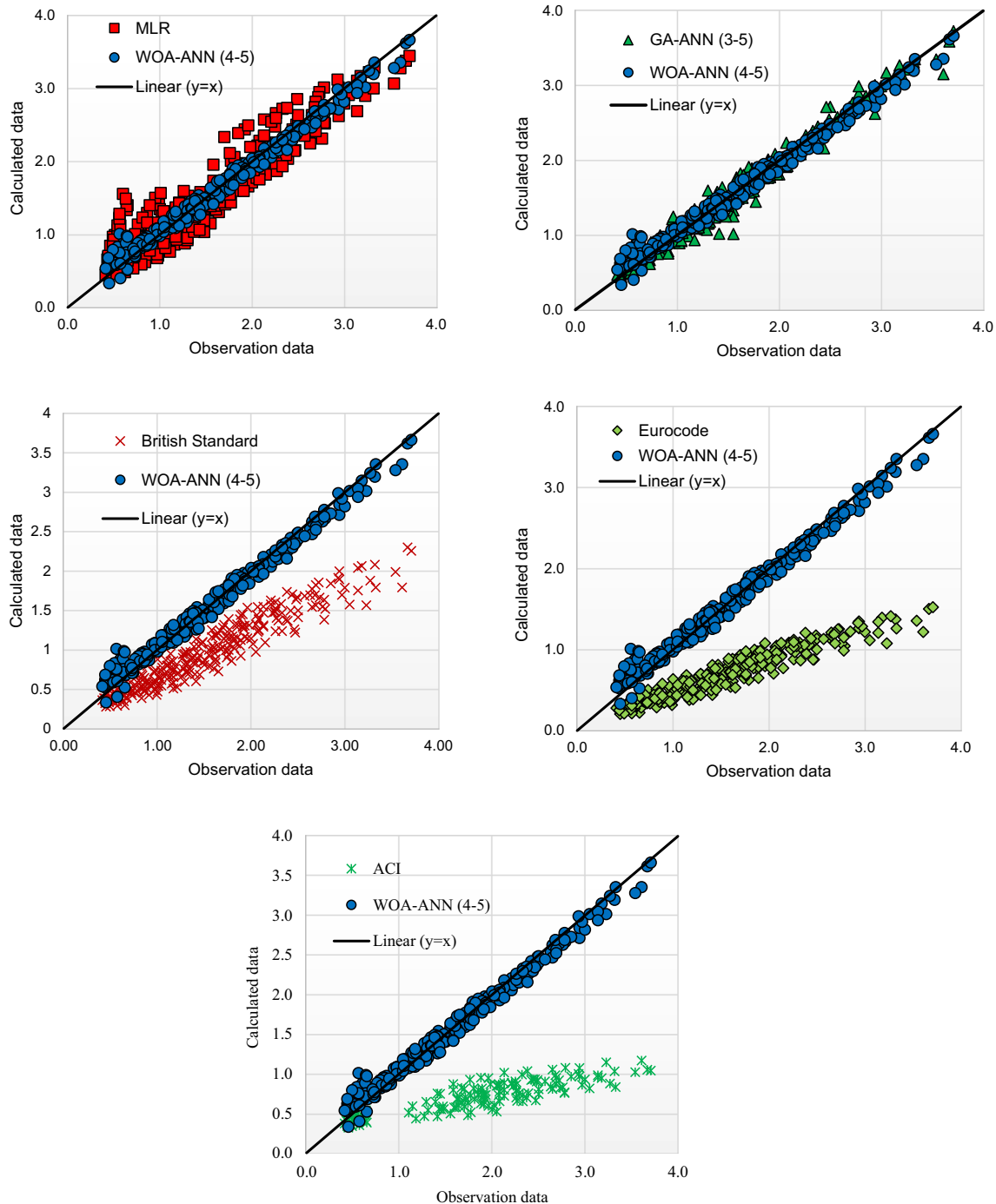
Fig. 8 Comparison between experimental and theoretical models for the overall deflection of RC beams

Table 10 Statistics of the various models on all datasets for creep and shrinkage deflection

Model	MSE	MARE	VAF%	R^2
WOA-ANN 2L(4–5)	0.012	0.082	98%	0.9858
Multiple linear regression (MLR)	0.077	0.204	87%	0.8671
GA-ANN 2L(3–5)	0.016	0.079	97%	0.9735
British standard	0.453	0.354	79%	0.9131
Eurocode	0.955	0.531	61%	0.9121
ACI	1.651	0.759	49%	0.7514

of *VAF* and R^2 of the WOA-ANN model were closest to unity, indicating a very good and robust prediction performance.

Another visual representation of the comparison of the performance of the hybrid WOA-ANN model against the other models and the international standard models can be provided by the Taylor diagram, which is presented in Fig. 9. This diagram depicts a graphical illustration of each model's adequacy based on the root mean-square-centered difference, the correlation coefficient, and the standard deviation. The results indicate that the closest prediction of the overall deflection to the point representing the actual experimental deflection due to shrinkage and creep is the WOA-ANN model proposed in this study, followed by the GA-ANN model. The ACI 318 model resulted in higher values of root mean-square-centered difference and standard deviation, indicating a rather low accuracy model in estimating the experimental data than the Eurocode and BS code models.

4 Sensitivity analysis of overall deflection to geometrical and mechanical parameters

In this section, a sensitivity analysis of the overall deflection resulted from shrinkage and creep to the geometrical and mechanical parameters (GGBFS content, f_c', the magnitude of sustained load, area of tensile reinforcement, and time) is conducted using the WOA-ANN model. The Sensitivity analysis (SA) reveals how significantly the model output is affected by changes within the input variables. There are two main types of SA: global and local sensitivity analysis. Local sensitivity analysis concentrates

Fig. 9 Taylor diagram visualization of the predictions of the various models
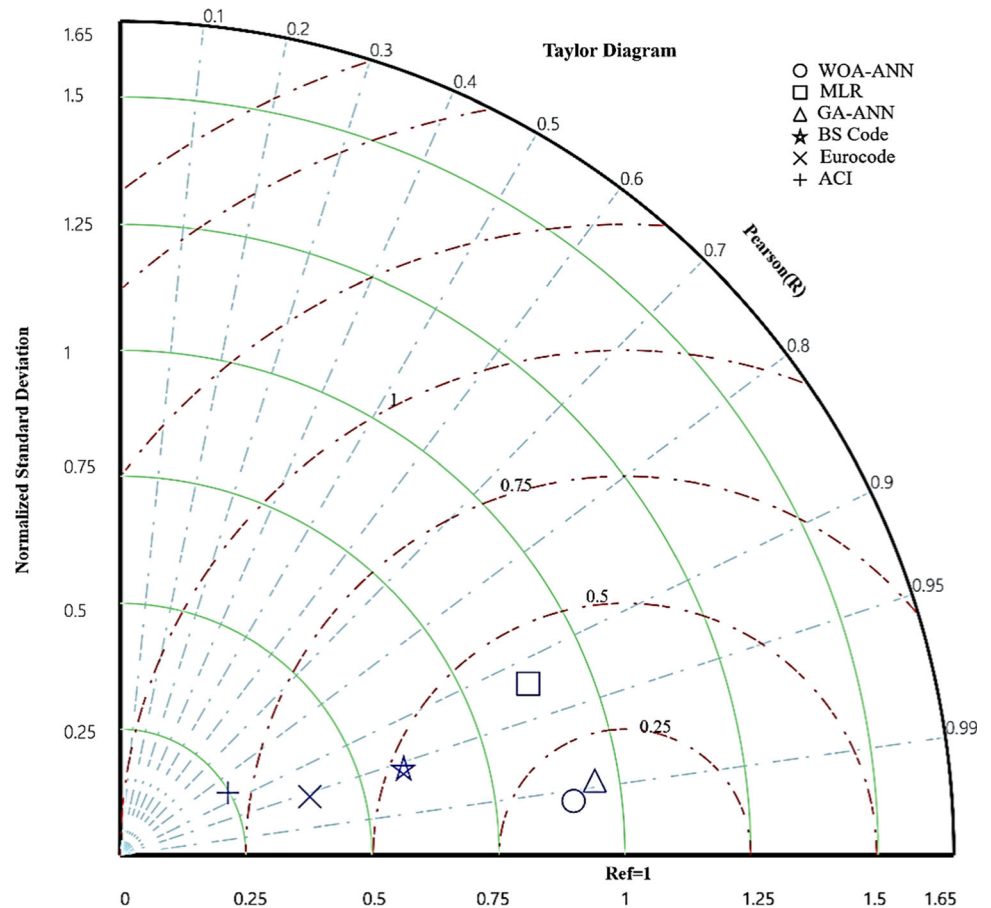
on the local impact of individual input parameters on the overall performance. Global sensitivity analysis (GSA) evaluates the influence of individual input parameters over their entire spatial range and measures the uncertainty of the overall performance (output) caused by input uncertainty, either in interaction with other parameters, or individually [67]. Therefore, considering the nature of the complex nonlinear behavior of the V_n parameter in this study, GSA was considered as the best option for investigating the impact of input parameters on the overall model performance.

Among GSA methods, variance-based approaches have been widely used in the literature for sensitivity analysis. The method provides a specific methodology for defining total and first-order sensitivity indices for each ANN model input parameter. Assuming a model of the form $Y = f(X_1, X_2,\ldots, X_k)$ where Y is a scalar, the variance-based technique takes a variance ratio to evaluate the impact of individual parameters using variance decomposition according to the following equation:

$$V = \sum_{i=1}^{k} V_i + \sum_{i=1}^{k}\sum_{j>i}^{k} V_{ij} + \cdots + V_{1,2,\ldots,k} \tag{15}$$

where V is the variance of the ANN model output, V_i is the first-order variance for the input X_i, and V_{ij} to $V_{1,2,\ ...,\ k}$ corresponds to the variance of the interaction of the k parameters. V_i and V_{ij}, which denote the significance of the individual input to the variance of the output, are a function of the conditional anticipation variance, according to the following equation

$$V_i = V_{xi}(E_{x\sim i}(YX_i)) \tag{16}$$

$$V_{ij} = V_{xixj}(E_{x\sim i}(YX_i, X_j)) - V_i - V_j \tag{17}$$

where $X_{\sim i}$ designates the set of all input variables apart from X_i. The first-order sensitivity index (S_i) represents the first-order impact of an input X_i on the overall output provided by the following equation.

$$S_i = \frac{V_i}{V(Y)} \tag{18}$$

The above-mentioned methodology for calculating the first-order sensitivity index was considered in this study. The results of the SA are presented in Fig. 10. Apart from the time parameter, the results indicate that the GGBFS content had the major influence, while the area of tensile reinforcement and f_c' have the least effect on the output parameter (i.e., the overall deflection). The magnitude of the sustained load can be classified as the second most influential input variable.
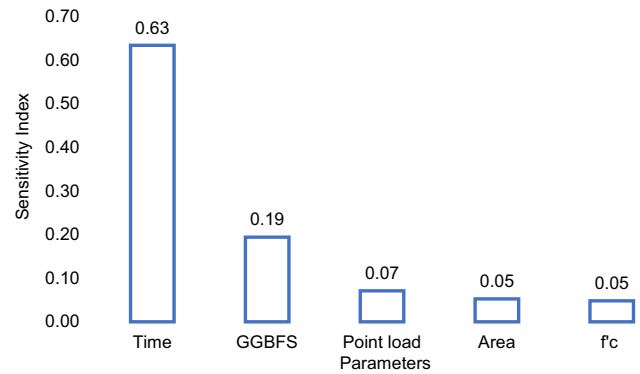
Fig. 10 Sensitivity of the overall deflection to geometrical and mechanical parameters

5 Conclusions

This research work investigated the creep and shrinkage deflection of RC beams containing different percentages of GGBFS at different ages, between 1 to 150 days. The empirical equations recommended by the international standards for estimating short and long-term deflections of RC beams due to creep and drying shrinkage were examined and discussed. In addition, a hybrid artificial neural network coupled with a metaheuristic Whale optimization algorithm was developed to estimate the overall deflection in RC beams due to shrinkage and creep, based on experimental data. The main findings of this study are summarized below.

- On average, shrinkage was responsible for around 12% of the overall deflection of RC beams regardless of binder constituents.
- The rate of the overall deflection was increased by increasing the GGBFS content where at the age of 150 days, the overall deflection of RC beam containing 60% GGBFS was 72% higher than the one of the OPCC-based beam.
- By increasing the reinforcement ratio (ρ) from 0.77 to 1.21%, the overall deflection was increased by an average of 17%. Such an increase is more evident in design mixes that contain high GGBFS content.
- Various statistical metrics were calculated and examined to compare the overall deflection of RC beams, versus the corresponding values predicted by the various models. The results confirmed that the proposed informational WOA-ANN model attained the most reliable and robust results for the determination of the overall deflection of RC beams. The *MSE* and *MARE* values were estimated as 0.012 and 0.082, respectively, indicating superior accuracy of the proposed WOA-ANN model that can achieve more reliable predictions of the overall deflection. This powerful feature

simplifies the design and provides a more generalized process for future generative design driven by artificial intelligence.

- The sensitivity analysis results indicate that apart from the time passed, the GGBFS content has the major influence on overall deflection, while the area of tensile reinforcement and $f_c^{'}$ have a minor contribution. The magnitude of the sustained load can be classified as the second most influential variable on the overall deflection.

Declarations

Conflict of interest The authors declare no conflict of interest.

References

1. Huseien GF et al (2017) Geopolymer mortars as sustainable repair material: a comprehensive review. Renew Sustain Energy Rev 80:54–74
2. García-Lodeiro I et al (2011) Compatibility studies between NASH and CASH gels Study in the ternary diagram Na$_2$O–CaO–Al$_2$O$_3$–SiO$_2$–H$_2$O. Cem Concr Res 41(9):923–931
3. Abdel-Gawwad H et al (2018) Recycling of concrete waste to produce ready-mix alkali activated cement. Ceram Int 44(6):7300–7304
4. Huseien GF, Shah KW, Sam ARM (2019) Sustainability of nanomaterials based self-healing concrete: An all-inclusive insight. J Build Eng
5. Huseien GF et al (2015) Synthesis and characterization of self-healing mortar with modified strength J Teknologi 76(1).
6. Sivakrishna A et al (2020) Green concrete: a review of recent developments. Mater Today: Proc 27:54–58
7. Asteris PG et al (2019) Investigation of the mechanical behaviour of metakaolin-based sandcrete mixtures. Eur J Environ Civ Eng 23(3):300–324
8. Amer I et al (2021) Characterization of alkali-activated hybrid slag/cement concrete. Ain Shams Eng J 12(1):135–144
9. Huseien GF et al (2019) Utilizing spend garnets as sand replacement in alkali-activated mortars containing fly ash and GBFS. Constr Build Mater 225:132–145
10. Tzevelekou T et al (2020) Valorization of slags produced by smelting of metallurgical dusts and lateritic ore fines in manufacturing of slag cements. Appl Sci 10(13):4670
11. Pujadas P et al (2017) The need to consider flexural post-cracking creep behavior of macro-synthetic fiber reinforced concrete. Constr Build Mater 149:790–800
12. Manzi S, Mazzotti C, Bignozzi MC (2017) Self-compacting concrete with recycled concrete aggregate: Study of the long-term properties. Constr Build Mater 157:582–590
13. Zhu L et al (2020) Experimental and numerical study on creep and shrinkage effects of ultra high-performance concrete beam. Compos Part B Eng 184:107713
14. Sumajouw D et al (2005) Behaviour and strength of reinforced fly ash-based geopolymer concrete beams. In: Australian structural engineering conference 2005. Engineers Australia
15. Collins F, Sanjayan JG (2000) Cracking tendency of alkali-activated slag concrete subjected to restrained shrinkage. Cem Concr Res 30(5):791–798
16. Li J, Yao Y (2001) A study on creep and drying shrinkage of high performance concrete. Cem Concr Res 31(8):1203–1206
17. Nassif H, Suksawang N, Mohammed M (2003) Effect of curing methods on early-age and drying shrinkage of high-performance concrete. Transp Res Rec 1834(1):48–58
18. Zhang J, Han YD, Gao Y (2014) Effects of water-binder ratio and coarse aggregate content on interior humidity, autogenous shrinkage, and drying shrinkage of concrete. J Mater Civ Eng 26(1):184–189
19. Güneyisi E, Gesoğlu M, Mermerdaş K (2008) Improving strength, drying shrinkage, and pore structure of concrete using metakaolin. Mater Struct 41(5):937–949
20. Leemann A, Lura P, Loser R (2011) Shrinkage and creep of SCC—the influence of paste volume and binder composition. Constr Build Mater 25(5):2283–2289
21. Huo XS, Al-Omaishi N, Tadros MK (2001) Creep, shrinkage, and modulus of elasticity of high-performance concrete. Mater J 98(6):440–449
22. Zhou W, Kokai T (2010) Deflection calculation and control for reinforced concrete flexural members. Can J Civ Eng 37(1):131–134
23. Marí AR, Bairán JM, Duarte N (2010) Long-term deflections in cracked reinforced concrete flexural members. Eng Struct 32(3):829–842
24. Mendis AS, Al-Deen S, Ashraf M (2017) Effect of rubber particles on the flexural behaviour of reinforced crumbed rubber concrete beams. Constr Build Mater 154:644–657
25. Xu T, Castel A, Gilbert RI (2018) On the reliability of serviceability calculations for flexural cracked reinforced concrete beams. In: Structures. Elsevier, Amsterdam
26. Hariche L et al (2012) Effects of reinforcement configuration and sustained load on the behaviour of reinforced concrete beams affected by reinforcing steel corrosion. Cem Concr Compos 34(10):1202–1209
27. Mias C et al (2013) Effect of material properties on long-term deflections of GFRP reinforced concrete beams. Constr Build Mater 41:99–108
28. Shariq M, Abbas H, Prasad J (2019) Effect of magnitude of sustained loading on the long-term deflection of RC beams. Arch Civil Mech Eng 19:779–791
29. Shariq M, Prasad J, Abbas H (2013) Long-term deflection of RC beams containing GGBFS. Mag Concr Res 65(24):1441–1462
30. Shariq M, Abba H, Prasad J (2017) Effect of GGBFS on time-dependent deflection of RC beams. Comput Concr 19(1):51–58
31. Un CH (2017) Creep behaviour of geopolymer concrete. Swinburne University of Technology

32. Han B, Xiang T-Y, Xie H-B (2017) A Bayesian inference framework for predicting the long-term deflection of concrete structures caused by creep and shrinkage. Eng Struct 142:46–55

33. Al-Zwainy FM et al (2018) Validity of artificial neural modeling to estimate time-dependent deflection of reinforced concrete beams. Cogent Eng 5(1):1477485

34. Zhu J, Wang Y (2021) Convolutional neural networks for predicting creep and shrinkage of concrete. Constr Build Mater 306:124868

35. Nguyen H et al (2021) Prediction of long-term deflections of reinforced-concrete members using a novel swarm optimized extreme gradient boosting machine. Eng Comput 1–13

36. Plevris V, Tsiatas G (2018) Computational structural engineering: past achievements and future challenges. Front Built Environ 4(21):1–5

37. Mohapatra P, Das KN, Roy S (2017) A modified competitive swarm optimizer for large scale optimization problems. Appl Soft Comput 59:340–362

38. Sun Y, Yang T, Liu Z (2019) A whale optimization algorithm based on quadratic interpolation for high-dimensional global optimization problems. Appl Soft Comput 85:105744

39. Luo J, Shi B (2019) A hybrid whale optimization algorithm based on modified differential evolution for global optimization problems. Appl Intell 49(5):1982–2000

40. Plevris V, Papadrakakis M (2011) A hybrid particle swarm—gradient algorithm for global structural optimization. Comput Aided Civ Infrastruct Eng 26(1):48–68

41. Kaur G, Arora S (2018) Chaotic whale optimization algorithm. J Comput Des Eng 5(3):275–284

42. Mirjalili S, Lewis A (2016) The Whale optimization algorithm. Adv Eng Softw 95:51–67

43. Gharehchopogh FS, Gholizadeh H (2019) A comprehensive survey: Whale Optimization Algorithm and its applications. Swarm Evol Comput 48:1–24

44. 318 AC (2020) Building code requirements for structural concrete (ACI 318-19): an ACI standard; Commentary on Building Code Requirements for Structural Concrete (ACI 318R-19). American Concrete Institute

45. Standard B (1997) BS 8110: Structural Use of Concrete, Part 1. Code of Practice for Design and Construction, BSI

46. En B (1992) 1-1: 2004 Eurocode 2: Design of concrete structures. General rules and rules for buildings, pp 1992–1993

47. Branson DE, Christiason M (1971) Time dependent concrete properties related to design-strength and elastic properties, creep, and shrinkage. Special Publ 27:257–278

48. Bhatt P, MacGinley TJ, Choo BS (2005) Reinforced concrete design: design theory and examples. CRC Press

49. 383 I (1970) Specification for coarse and fine aggregates from natural sources for concrete. Bureau of Indian Standards

50. 6 IP (1988) Methods of physical tests for hydraulic cement. Bureau of Indian Standards

51. IS (1989) Specification for 43-grade Ordinary Portland Cement. Bureau of Indian Standard New Delhi, India

52. Standard I (2000) Plain and reinforced concrete-code of practice. Bureau of Indian Standards, New Delhi

53. BIS (1999) IS 12089: Indian standard specifications for granulated slag for the manufacture of Portland slag cement. BIS New Delhi, India

54. Shariq M, Prasad J, Masood A (2010) Effect of GGBFS on time dependent compressive strength of concrete. Constr Build Mater 24(8):1469–1478

55. Plevris V (2009) Innovative computational techniques for the optimum structural design considering uncertainties. National Technical University of Athens, Athens, Greece, p 312

56. Adeli H (2001) Neural networks in civil engineering: 1989–2000. Comput Aided Civ Infrastruct Eng 16(2):126–142

57. Flood I, Kartam N (1994) Neural networks in civil engineering. I: principles and understanding. J Comput Civ Eng 8(2):131–148

58. Seghier MEAB et al (2021) On the modeling of the annual corrosion rate in main cables of suspension bridges using combined soft computing model and a novel nature-inspired algorithm. Neural Comput Appl 1–17

59. Nikoo M et al (2018) Determining the natural frequency of cantilever beams using ANN and heuristic search. Appl Artif Intell 32(3):309–334

60. Haykin S (2007) Neural networks: a comprehensive foundation. Prentice-Hall, Inc., Englewood Cliffs

61. Bishop CM (2006) Pattern recognition and machine learning. Springer, Berlin

62. Watkins WA, Schevill WE (1979) Aerial observation of feeding behavior in four baleen whales: Eubalaena glacialis, Balaenoptera borealis, Megaptera novaeangliae, and Balaenoptera physalus. J Mammal 60(1):155–163

63. Goldbogen JA et al (2013) Integrative approaches to the study of baleen whale diving behavior, feeding performance, and foraging ecology. Bioscience 63(2):90–100

64. Guha D, Roy PK, Banerjee S (2020) Whale optimization algorithm applied to load frequency control of a mixed power system considering nonlinearities and PLL dynamics. Energy Syst 11(3):699–728

65. Sadowski Ł et al (2019) The nature-inspired metaheuristic method for predicting the creep strain of green concrete containing ground granulated blast furnace slag. Materials 12(2):293

66. Bowden GJ, Dandy GC, Maier HR (2005) Input determination for neural network models in water resources applications. Part 1—background and methodology. J Hydrol 301(1–4):75–92

67. Saltelli A et al (2008) Global sensitivity analysis: the primer. Wiley, London